Journal of Geophysical Research: Solid Earth

RESEARCH ARTICLE
10.1029/2017JB015357

Key Points:
- Lapilli and bombs from Surtseyan eruptions show gradual textural variations due to the quenching in water
- The kinetics of magma cooling during Surtseyan eruptions are influenced by particle size, radial position, and Leidenfrost effect
- The 3-D analysis of vesicle metrics using X-ray microtomography allows quantification of the percolation threshold in volcanic rocks

Supporting Information:
- Supporting Information S1

Correspondence to:
M. Colombier,
mathieu.colombier@min.uni-muenchen.de

Citation:
Colombier, M., Scheu, B., Wadsworth, F. B., Cronin, S., Vasseur, J., Dobson, K. J., et al. (2018). Vesiculation and quenching during Surtseyan eruptions at Hunga Tonga-Hunga Ha'apai volcano, Tonga. *Journal of Geophysical Research: Solid Earth*, *123*, 3762–3779. https://doi.org/10.1029/2017JB015357

Received 14 DEC 2017
Accepted 6 MAY 2018
Accepted article online 15 MAY 2018
Published online 31 MAY 2018

Vesiculation and Quenching During Surtseyan Eruptions at Hunga Tonga-Hunga Ha'apai Volcano, Tonga

M. Colombier[1], B. Scheu[1], F. B. Wadsworth[1], S. Cronin[2], J. Vasseur[1], K. J. Dobson[3], K.-U. Hess[1], M. Tost[2], T. I. Yilmaz[1], C. Cimarelli[1], M. Brenna[4], B. Ruthensteiner[5], and D. B. Dingwell[1]

[1]Department of Earth and Environmental Sciences, Ludwig-Maximilians-Universität München, Munich, Germany, [2]School of Environment, University of Auckland, Auckland, New Zealand, [3]Department of Earth Sciences, University of Durham, Durham, UK, [4]Department of Geology, University of Otago, Dunedin, New Zealand, [5]Bavarian State Collection of Zoology, Munich, Germany

Abstract Surtseyan eruptions are shallow to emergent subaqueous explosive eruptions that owe much of their characteristic behavior to the interaction of magma with water. The difference in thermal properties between water and air affects the cooling and postfragmentation vesiculation processes in magma erupted into the water column. Here we study the vesiculation and cooling processes during the 2009 and 2014–2015 Surtseyan eruptions of Hunga Tonga-Hunga Ha'apai volcano by combining 2-D and 3-D vesicle-scale analyses of lapilli and bombs and numerical thermal modeling. Most of the lapilli and bombs show gradual textural variations from rim to core. The vesicle connectivity in the lapilli and bombs increases with vesicularity from fully isolated to completely connected and also increases from rim to core in transitional clasts. We interpret the gradual textural variations and the connectivity-vesicularity relationships as the result of postfragmentation bubble growth and coalescence interrupted at different stages by quenching in water. The measured vesicle size distributions are bimodal with a population of small and large vesicles. We interpret this bimodality as the result of two nucleation events, one prefragmentation with the nucleation and growth of large bubbles and one postfragmentation with nucleation of small vesicles. We link the thermal model with the textural variations in the clasts—showing a dependence on particle size, Leidenfrost effect, and initial melt temperature. In particular, the cooling profiles in the bombs are consistent with the gradual textural variations from rim to core in the clasts, likely caused by variations in time available for vesiculation before quenching.

1. Introduction

Surtseyan eruptions owe many of their characteristics to the interaction of magma with water and were named after the 1963–1964 eruption forming Surtsey Island in Iceland (Walker & Croasdale, 1971). The fragmentation and vesiculation of pyroclasts during these eruptions are modified by the abundance of water, which has different physical properties compared with air and eruptive gases—the typical eruptive media of subaerial volcanism.

Vesiculation during a volcanic eruption is driven by exsolution of volatile phases that become supersaturated in magma. This can principally be driven by decompression (e.g., Sparks, 1978) or heating (e.g., Lavallée et al., 2015). The process proceeds through bubble nucleation (Gonnermann & Gardner, 2013), growth (Proussevitch & Sahagian, 1998), and coalescence (Nguyen et al., 2013). The onset of bubble connectivity (creating permeability) occurs at the percolation threshold, the vesicularity at which bubble coalescence is system spanning (cf Colombier et al., 2017). The percolation threshold of a vesiculating system depends on the bubble size distribution, the degree of shearing deformation, crystallinity, surface tension, occurrences of local brittle failure (Blower, 2001; Burgisser et al., 2017; Colombier et al., 2017; Kushnir et al., 2017; Lindoo et al., 2017; Okumura et al., 2008; Spina et al., 2016) and can have a broad range of values from 0.2 to >0.7 (e.g., Colombier et al., 2017). Vesiculation commonly starts during magma ascent in the conduit (prefragmentation) and continues after ejection of tephra until quenching (postfragmentation). The timing of vesiculation and quenching is dependent on the nature of the coolant (air, vapor film, or liquid water), on the radial distance between magma and this cooling media, and on the clast sizes (Kueppers et al., 2012; Wilding et al., 2000).

In subaqueous settings, some prefragmentation vesiculation may be hindered by water pressure (e.g., I. C. Wright et al., 2003), and postfragmentation vesiculation of ejected pyroclasts may be quickly interrupted by quenching in water. Magma cooling rates in water are typically higher than in air. This is especially true for deepwater eruptions where envelopes of steam formed around magma surfaces rapidly collapse and enable direct magma-water contact. This is thought to generate the highest cooling rates known for silicate glass, such as Limu o Pelé (bubble wall fragments) or basaltic bombs in deep submarine settings (Kueppers et al., 2012; Nichols et al., 2009; Potuzak et al., 2008). Efficient magma cooling by water impedes postfragmentation bubble growth (e.g., Liu et al., 2005), and coalescence, producing dense clasts (e.g., Schipper et al., 2011). Under shallow water (<200 m) during Surtseyan eruptions, magma can be insulated from direct contact with water by a steam cupola (Kokelaar, 1986). Thus, quenching may not be as rapid as in the deep water case, and vesiculation may be less affected. This could explain high vesicularities commonly found in tephra from Surtseyan eruptions (e.g., Murtagh & White, 2013).

In this study, we investigate the relationship between cooling and vesiculation processes during Surtseyan eruptions. By examining the internal structure of the pyroclasts, we shed light on the vesiculation processes and estimate the percolation threshold in lapilli and bombs from the 2009 and 2014–2015 Surtseyan eruptions of Hunga Tonga-Hunga Ha'apai volcano. We then propose a conceptual generalizable framework for explaining the first-order relationships between quenching and vesiculation for these types of eruptions by comparison with a 1-D solution to the heat equation.

2. Geological Context

The islands of Hunga Tonga and Hunga Ha'apai are located ~67 km north-northwest of Nuku'alofa, Kingdom of Tonga. They are part of the intraoceanic Tonga-Kermadec arc (Figure 1), formed as a result of subduction of the Pacific Plate beneath the Australian plate (e.g., Ewart et al., 1998). The two islands are remnants of the rim of a roughly 3- to 4-km-large submarine caldera (Figure 1b). In various parts of the caldera, eruptions were noted in 1912, 1938, and 1988, with the best recorded being Surtseyan eruptions forming tuff cones in separate locations in 2009 and 2014–2015 (Bohnenstiehl et al., 2013; W. B. Bryan et al., 1972; Global Volcanism Program, 1988, 2009a, 2009b, 2015; Vaughan & Webley, 2010).

The 2009 eruption lasted from 17 to 21 March 2009 and formed two subaerial tuff cones on the northwestern and southern sides of Hunga Ha'apai (Vaughan & Webley, 2010). The eruption was characterized by steam and ash plumes rising up to ≤7.6 km asl and posing hazards to local air traffic, with base surges and debris jets observed from three individual vents, (Bohnenstiehl et al., 2013; Global Volcanism Program, 2009a, 2009b; Vaughan & Webley, 2010). The newly formed tuff cones were quickly eroded by waves once activity had ceased. At the time of sampling in November 2015, only a small remnant of the cone located on the western site of Hunga Ha'apai was still preserved above the water surface.

The 2014–2015 eruption occurred between 19 September 2014 and 24 January 2015 and formed an ~120-m-high and 2-km-wide near-circular tephra cone which coalesced with the two preexisting islands of Hunga Tonga and Hunga Ha'apai. The eruption did not produce much distal ash, but steam plumes up to 10 km-high were observed, causing cancellation of international flights on 13 and 14 January (Global Volcanism Program, 2015). The edifice was constructed within ~10 days by vigorous tephra jets (≤750 m asl) and base surges extending radially more than 1 km away from the vent (Global Volcanism Program, 2015).

Most samples analyzed in this study were collected from proximal fall/jet deposits sampled from the main cone formed during the 2014–2015 eruption, with one clast collected from surge deposits beyond the main cone (Figure 1d). In addition, two bombs were sampled from the proximal fall/debris jet deposits of the 2009 tuff cone formed at the northwestern flank of Hunga Ha'apai (Figure 1d). The whole rock compositions of the 2009 and 2014–2015 magmas are similar with a basaltic andesitic to andesitic composition (Table S1 in supporting information). The glass composition of a bomb from the 2014–2015 eruption is andesitic (Table S1 in supporting information).

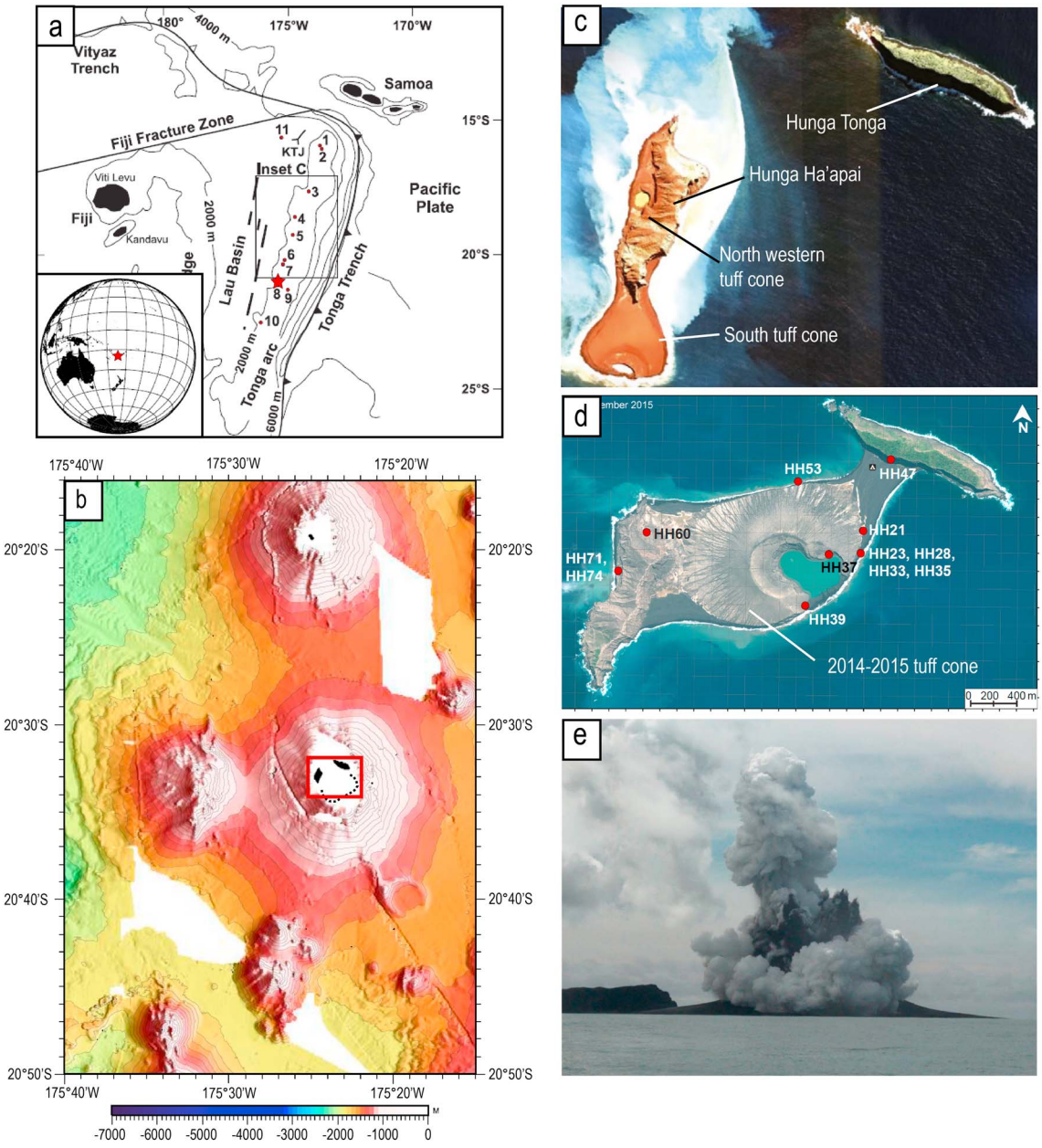

Figure 1. Geological setting of the 2009 and 2014–2015 Surtseyan eruptions at Hunga Tonga-Hunga Ha'apai volcano. (a) Map representing the intraoceanic Tonga arc in its regional tectonic setting and the location of the Hunga Tonga-Hunga Ha'apai volcano marked with a red star (modified after Bohnenstiehl et al., 2013 and S. E. Bryan et al., 2004). (b) Bathymetry of the area showing the Hunga Ha'apai and Hunga Tonga islands (in the red box) at the rims of a preexisting caldera (black dashed line). (c) Google Earth image of the islands after the 2009 eruptions. Two vents and associated tuff cones at the northwestern and south sides of Hunga Ha'apai are visible. (d) Google Earth image showing the Hunga Ha'apai-Hunga Tonga volcano after the 2014–2015 eruption and the presence of the newly formed tuff cone. The location of the samples used in this study is marked by a red solid circle. Most of the samples come from the 2014–2015 eruption except samples HH71 and 74 that come from the 2009 northwestern tuff cone. (e) Typical example of a steam and ash plume during the 2014–2015 eruption (picture courtesy of New Zealand High Commission in Nuku'alofa).

3. Materials and Methods

We analyzed 21 juvenile lapilli and 10 bombs from the 2009 and 2014–2015 eruptions. On a subset of these clasts, we measured vesicle size distributions (VSDs) and number densities using scanning electron microscopy (SEM) and X-ray computed microtomography (XCT). The vesicularity and vesicle connectivity of the juvenile lapilli and bombs were estimated combining Helium pycnometry and XCT. We also used thermal

Table 1
Textural Analysis Using SEM (2-D) and XCT (3-D) and Other Standard methods (See Text for Details)

Sample name Sample type	HH37-3 Transitional (whole clast)	HH37-3 Transitional (dense subsample)	HH37-4 Dense lapillus	HH28-3 Dense lapillus	B74 Dense bomb	B71 Vesicular core bomb
Vesicularity (Archimedes)	0.40	—	0.48	—	0.27	0.85
Vesicularity (2-D)	—	0.21	0.32	—	0.23	0.7
Vesicularity 3-D	—	0.21	0.41	0.26	—	0.85
Connectivity (pycnometry)	0.43	—	0.66	—	0.45	0.98
Connectivity (3-D)	—	0.09	0.88	0.33	-	1
Nv vesicles >4 μm 2-D analysis × 10^4 (mm^{-3})	—	0.67	x	—	1.42	x
Nv vesicles >4 μm 3-D analysis × 10^4 (mm^{-3})	—	0.73	x	1.38	—	x
Distribution (2-D)	—	Unimodal	x	—	Bimodal	x
Distribution (3-D)	—	Bimodal	x	Bimodal	—	x

Note. Nv = vesicle number density. x = the 2-D vesicle size distribution and vesicle number density were not determined because of high vesicle connectivity. SEM = scanning electron microscopy; XCT = X-ray computed tomography.

analysis and modeling, based on heat transfer equations allowing us to link textural features to cooling processes.

3.1. The 2-D Image Analysis

We studied the 2-D textures of three lapilli clasts and two bomb clasts using backscattered electron images collected on a HITACHI SU 5000 Schottky FE-SEM. We used the image nesting strategy presented by Shea et al. (2010), taking images at different magnifications (25X, 100X, and 250X) in order to image the range of vesicle size in all samples. These 2-D images were binarised using Adobe Photoshop© and analyzed using FOAMS (MATLAB user interface developed by Shea et al. (2010) in order to retrieve the 2-D vesicularity, the VSD, and vesicle number density through 2-D to 3-D stereological conversion (results presented in Table 1). We only measured the VSD and number density in samples with low vesicle connectivity, because the 2-D image analysis process is not well suited to highly interconnected pore networks. In samples with high connectivity, we only measured the 2-D vesicularity since this is a bulk metric that is not dependent on the pore geometries.

3.2. Pycnometry Measurements

The 21 juvenile lapilli and 10 bomb samples from different stratigraphic units and showing macroscopically a broad textural variability were examined for bulk density analysis. Bombs were cored to 2-cm diameter and 2-cm-long cylinders, whereas the lapilli were analyzed as a whole. We determined the sample density using the Archimedes principle for irregular lapilli samples and using the geometrical volume for the cylinders (Table 2). The densities of three pore-free lapilli and bombs were measured by powdering them and using He-pycnometry. He-pycnometry measurements were performed using a Quantachrome® Ultrapyc 1200e (Table 2). These solid densities were within 0.38% of each other for all samples; therefore, we assumed that the average of these solid densities was representative of all populations of lapilli and bombs. Based on these values, the bulk density was converted into a bulk vesicularity Φ. The connected vesicularity Φ_{con} (or He-accessible volume) of the samples was also measured by He-pycnometry (Table 2). The pycnometry-defined connectivity (denoted C_1) was obtained by dividing the connected vesicularity by the bulk vesicularity (Colombier et al., 2017). C_1 is the measure of the fraction of the vesicles that reach the external surface of the sample, although these vesicles may not necessarily extend through the whole sample. In section 3.4, we discuss the differences between the various definitions of connectivity.

3.3. The 3-D Image Analysis

Five lapilli of 4- and 32-mm diameter were analyzed by X-ray computed tomography (XCT) to measure their 3-D porosimetric properties and to compare these with laboratory measurements and 2-D textural analysis. Lapilli with a broad range of vesicularity and connectivity (predetermined by pycnometry) were chosen for the XCT analysis. XCT data are unique in their ability to fully resolve the 3-D connectivity (within the spatial resolution of the imaging) as no manual rectification is needed, and the true geometry of complex interacting vesicles can be quantified. The small lapilli were entirely scanned, while large lapilli were cored to obtain a

Table 2
Density, Bulk, and Connected Vesicularity and C_1 Connectivity for the Lapilli and Bombs, as Measured by the Archimedes Method and by Helium Pycnometry

Sample type	Deposit type	Sample name	Density	Bulk vesicularity Φ_b	Connected vesicularity Φ_{con}	Connectivity C_1
Lapilli	Fall	HH37-1	1.52	0.45	0.22	0.47
	Fall	HH37-2	1.24	0.55	0.52	0.91
	Fall	HH37-3	1.70	0.38	0.18	0.43
	Fall	HH37-4	1.48	0.46	0.32	0.66
	Fall	HH33-1	1.68	0.39	0.19	0.47
	Fall	HH33-2	1.28	0.53	0.51	0.93
	Fall	HH33-3	1.40	0.49	0.38	0.75
	Fall	HH33-4	1.59	0.42	0.23	0.53
	Fall	HH23-1	0.31	0.89	0.88	0.99
	Fall	HH23-6	1.47	0.47	0.34	0.70
	Fall	HH23-5	1.80	0.35	0.13	0.35
	Fall	HH21-b-1	1.38	0.50	0.50	0.98
	Fall	HH21-b-2	1.45	0.47	0.44	0.90
	Fall	HH21-b-3	1.29	0.53	0.54	0.99
	Fall	HH21-b-4	1.75	0.36	0.16	0.41
	Fall	HH21-b-5	1.28	0.53	0.54	0.98
	Fall	HH35-1	1.43	0.48	0.46	0.92
	Fall	HH35-2	1.54	0.44	0.43	0.93
	Fall	HH50-1	1.46	0.47	0.38	0.79
	Surge	HH60-1	1.31	0.52	0.52	0.97
	Fall	HH36-2	1.59	0.42	0.28	0.62
Bombs	Fall	B58[a]	1.54	0.46	0.42	0.91
	Fall	B58	1.53	0.46	0.42	0.91
	Fall	B52	1.90	0.33	0.27	0.80
	Fall	B53[a]	1.70	0.40	0.39	0.96
	Fall	B39[a]	1.44	0.49	0.47	0.96
	Fall	B29 rim[a]	1.22	0.57	0.51	0.88
	Fall	B29 core[a]	1.12	0.61	0.60	0.99
	Fall	B30rim[a]	1.29	0.55	0.49	0.90
	Fall	B30	0.84	0.71	0.70	0.99
	Fall	B57	1.75	0.39	0.37	0.97
	Fall	B71 core	0.43	0.85	0.82	0.97
	Fall	B74[a]	2.07	0.27	0.12	0.45

Note. Density measured using the geometrical volume of the cylinders.
[a]The samples in which the density was measured by geometry.

small cylindrical sample with a diameter of 5 mm. The volume of the cylinders was scaled to the largest vesicles observed. One bomb showing gradual textural variations from rim to core was also analyzed by XCT on cores of different diameters (2- to 3-mm diameter at the rim where vesicle sizes are small and 5–10 mm in the transitional region and in the core, where larger vesicles were observed).

Scanning was performed on a GE® Phoenix Nanotom m laboratory scanner, operating at 80–90 kV and 120–250 nA, using a 0.1- to 0.2-mm-thick Al filter to reduce beam hardening. Spatial voxel resolutions range from 1.2 to 2 μm depending on sample size (see Table 3 for specifics of each scan). Filter back projection reconstruction was performed using the GE® proprietary software and visualization and quantification performed using Avizo® (FEI). A full processing workflow including volume of interest (VOI) definition, filter settings, and error analysis is given in supporting information. After defining a representative cubic VOI (between 0.5 and 40 mm^3; see supporting information) and applying an edge preserving nonlocal means filter (Buades et al., 2011) to reduce image noise, a semiautomated grayscale-driven thresholding procedure was used to define each voxel as either vesicle or solid. Vesicularity was then defined by the fraction of the VOIs labeled as vesicles. Vesicle connectivity was assessed in three orthogonal directions and with varying the "connection geometry" between vesicles. Defining adjoining vesicles as connected when sharing a voxel face, edge, or corner showed little effect on throughgoing sample connectivity. The values measured for planar vesicle-vesicle connectivity are shown (Table 3). The connectivity definition C_2 corresponds to the fraction of the pores that extend across the sample (a definition more cognate with permeability measurements; Table 3). A number of

Table 3
Vesicularity (Φ) and C_1 and C_2 Vesicle Connectivity for the Lapilli and Bombs as Determined From XCT Data

Sample type	Stratigraphic unit	Deposit type	Sample	VOI (mm^3)	Vesicularity Φ	Connectivity C_2	Connectivity C_1	Pixel size (μm)	Filter	Voltage (kV)	Current (nA)	Timing (s)	Nb images
Lapilli	Surge sequence	Surge	HH47-1	7.58	0.54	1.00	1.00	1.82	0.1 al	90	170	1,000	1,201
	Surge sequence	Surge	HH47-2	3.01	0.64	0.99	0.99	1.55	0.2 al	90	170	1,000	1,440
	Unit 6	Fall	HH28-3	1.76	0.26	0.33[a]	0.61	1.55	0.2 al	90	170	1,000	1,440
	Unit 1	Fall	HH37-4	32.34	0.35	0.59	0.74	3.10	0.1 al	80	120	1,250	1,200
	Unit 2	Fall	HH37-3	13.48	0.21	0.09[a]	0.43	1.60	0.2 al	90	170	1,500	1,800
Bomb	2009 eruption	Fall	HH71rim1	1.08	0.32	0.82	0.89	1.20	0.1 al	80	250	2,000	2,000
	2009 eruption	Fall	HH71rim2	0.51	0.35	0.77	0.87	1.30	0.1 al	80	250	2,000	2,000
	2009 eruption	Fall	HH71trans1	10.56	0.70	1.00	1.00	1.82	0.1 al	90	170	2,000	2,000
	2009 eruption	Fall	HH71trans2	30.97	0.75	1.00	1.00	2.00	0.1 al	90	170	2,000	2,000
	2009 eruption	Fall	HH71core	37.60	0.85	1.00	1.00	2.00	0.1 al	90	170	2,000	2,000

Note. The volume of sample used for the analysis is also shown. XCT = X-ray computed tomography; VOI = volume of interest.
[a]Anisotropic samples in which vesicles are connected only in the x direction.

shape-specific automated feature separation methodologies could be applied to the 3-D data to separate vesicles (where spatial resolution is thought insufficient to resolve thin films), but to avoid any potential bias in the data caused by these methods, the volume of each vesicle and the vesicle number density were only measured (Table 3) on the clasts with low vesicle connectivity (previously measured by He-pycnometry).

3.4. Differences Between the Connectivity Definitions

Most connectivity data for volcanic rocks available in the literature were obtained using He-pycnometry, (C_1; Figure 2; see Colombier et al., 2017 for a compilation). However, the pycnometry definition of connectivity has a flaw, which is the fact that the vesicles connected to the exterior of the clast are treated as connected even when they do not extend throughout the whole sample. Pycnometry rarely finds low (typically $C_1 < 0.5$) connectivity, and it is therefore difficult to quantitatively assess the percolation threshold. The definition derived from the XCT data (the percolating connectivity, C_2) is the fraction of interconnected vesicles in a given flow direction (Figure 2): a definition more relevant for comparison with permeability analyses. It also allows investigation of very low connectivities and therefore better assess where the percolation threshold is crossed. This approach has only recently been adopted in volcanology (e.g., Couves et al., 2016; Vasseur & Wadsworth, 2017; Wadsworth, Vasseur, Llewellin, Dobson, et al., 2017). Another benefit from the XCT technique compared to pycnometry is that it provides information on the directionality of the connectivity (see Table 3). Finally, our tomography data were compared with literature data quantifying connectivity as the ratio of the largest vesicle cluster to the total vesicularity (C_3; Bai et al., 2010; Okumura et al., 2008; Polacci et al., 2008, 2012). In cases where a single, large interconnected vesicle network extends through the system (such as seen here), this definition is equivalent to C_2. In rare cases, several permeable vesicle clusters might be disconnected resulting in slight differences between C_2 and C_3.

The main caveat inherent to connectivity measurement using XCT rather than He-pycnometry is the small VOI analyzed. This has been tested in the tomography data (see supporting information). Care should be taken to avoid issues of scale dependence and unrepresentative volume choices. Variability in scan conditions (notably voxel resolution and image artifacts) and operator decision may also affect the CT data but can generally be avoided by systematic and consistent application of data driven algorithms or detailed error analysis on the entire workflow.

3.5. Thermal Analysis and Modeling

We estimated the glass transition temperature T_g on selected glassy ash particles (diameter of 500 μm) by heating them in a Netzsch® Pegasus 404C simultaneous thermal analyzer using a heating rate of 10°C/min up to a final temperature of 1000°C. We also analyzed the relative mass loss during the heating process and due to degassing of meteoritic and magmatic water present in the glass. The heat flow signal and the relative mass loss during heat treatment (Table S2 in supporting information) are shown in Figure 3. T_g was estimated to onset between 535 and 584°C (Figure 3a), and the total mass loss was 1.25 wt.% (Figure 3b), consistent with the losses during electron microprobe analysis of the glass phase (using a Jeol JXA-8230 Superprobe with a defocussed 10-μm beam at Victoria University of Wellington; Table S1 in supporting information). Measuring the mass loss after heating above T_g provides an estimation of the water content still dissolved in the glass (and therefore in the melt at the time of quenching) of about 1.01 wt.% (Figure 3b). For comparison, we also calculated T_g using a multicomponent viscosity model (Giordano et al., 2008) with the average glass composition and total H_2O content discussed above. The viscosity model predicts T_g = 546°C, which is consistent with the range measured by heat flow changes. The Vogel-Fulcher-Tammann parameters output by the viscosity model are $A = -4.55$, $B = 7300.7$, and $C = 378.6$ where the temperature is taken to be in kelvin (Giordano et al., 2008).

We assessed the evolution of the temperature distribution T in a particle of radius R using Fourier's law for diffusive heat transfer cast in 1-D spherical coordinates (Crank, 1975)

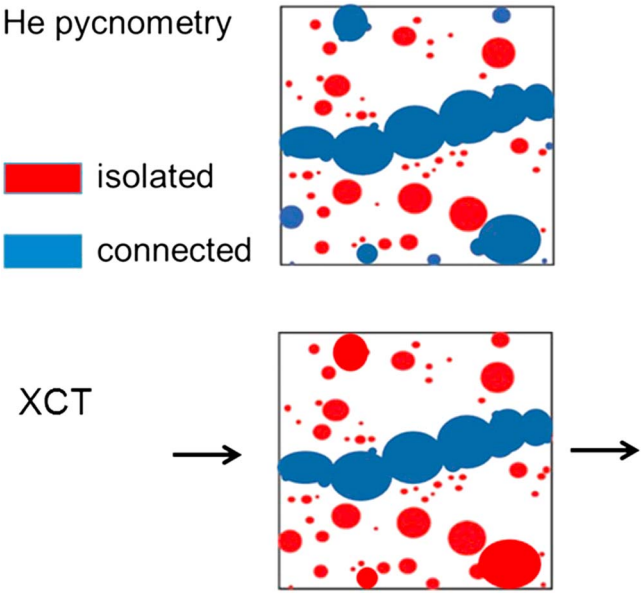

Figure 2. Sketch showing the differences between the definitions of vesicle connectivity used. The vesicles considered as connected or isolated in the different methods are colored in blue and red, respectively. (top) C_1as defined by He pycnometry in which all vesicles connected to the exterior of the sample are considered as connected. (bottom) C_2 as defined from the XCT data, in which only the vesicles that extend through the sample are considered connected. C_2 is more relevant for comparison with permeability measurements and for assessment of the percolation threshold. Arrows represent the direction of gas flow, which can be set by the user and was tested in all three orthogonal directions. XCT = X-ray computed tomography.

$$r^2\frac{\partial T}{\partial t}=\frac{\partial}{\partial r}\left(r^2D\frac{\partial T}{\partial r}\right) \tag{1}$$

where t is the time, r is the radial distance from the particle center, and D is the thermal diffusivity in the material.

The value of D is dependent on temperature and for silicate melts, and glasses can be predicted smoothly across the glass transition interval by

$$D=D_0\exp(\alpha T) \tag{2}$$

where D_0 is the extrapolated diffusivity at $T = 0$ and a function of Φ and α is a constant. For $\Phi = 0$ and by comparison with measurements from Bagdassarov and Dingwell (1994), Wadsworth, Vasseur, Llewellin, Genareau, et al. (2017) calibrated these two parameters in the range 550–1100°C as $D_0 = 1.88 \times 10^{-7}$ m^2/s and $\alpha = 1.58 \times 10^{-3}$ K^{-1}. $D_0(\Phi)$ is then given by (see Connor et al., 1997)

$$D_0(\Phi)=\frac{k(\Phi)}{\rho C_p(1-\Phi)+\Phi\rho_w C_{p,w}} \tag{3}$$

for which $k(\Phi) = D_0\rho C_p(1 - \Phi)/(1 + \Phi)$ is the vesicularity-dependent thermal conductivity (Bagdassarov & Dingwell, 1994), ρ and ρ_w are the melt and water densities respectively, and C_p and $C_{p,w}$ are the specific heat capacities. We used ρ = 2,200 kg/m^3 and C_p = 1,000 J·kg·K^{-}, and looked at R in the range 5–500 mm and Φ between 0.2 and 0.6. We solved the heat equation numerically by means of a fully implicit finite difference scheme (i.e., backward time, centered space) coupled with a relaxed fixed point method to ensure convergence at each time step (e.g., Wadsworth, Vasseur, Llewellin, Genareau, et al., 2017). We assumed that at $t = 0$ the particle is in thermal equilibrium at the initial melt temperature T_{mi}; $T(t = 0, r) = T_{mi}$. At the particle center we employ a Neumann boundary condition of 0 (i.e., boundary of insulation; $D\frac{\partial T}{\partial r}\big|_{r=0} = 0$) and at the rim we looked at two specific cases: (1) the temperature is instantaneously dropped to the surrounding water temperature T_w, $T(t, r = R) = T_w$, and (2) the temperature decreases according to convective and radiative heat exchange across the rim

$$D\frac{\partial T}{\partial r}\bigg|_{t,r=R}=\frac{\sigma\varepsilon}{\rho C_p}T^4+\frac{h}{\rho C_p}T \tag{4}$$

where σ is the Stefan-Boltzmann constant (5.67×10^{-8} W·m^{-2}·K^{-4}), ε the radiative emissivity, and h the convective heat transfer coefficient. In the case of (2) we used a convective heat transfer coefficient of h = 50 W·m^{-2}·K^{-1} (Stroberg et al., 2010) and a radiative emissivity of $\varepsilon = 0.9$ (Mastin, 2007). In this case, radiation was negligible so that the choice of ε makes little difference. We chose to track the time for T to reach the measured range of T_g in the particle. This is a first-order metric for the temperature where the particle is quenched to a glass, and therefore, vesiculation can no longer occur.

4. Results

4.1. Textural Classification of the Pyroclasts

On the basis of macroscopic observations of vesicle texture and vesicularity, the lapilli can be separated into three main textural types: (1) dense, (2) transitional, and (3) vesicular (Figure 4). The dense and transitional textural types are the most abundant and are also recognized internally within the bombs (Figures 4a–4c). The transitional lapilli and bombs exhibit textures with a gradual increase of vesicle size and degree of coalescence from rim to core (Figures 4b–4d). Large vesicles are more common in the vesicular cores of these clasts but can also be present in the dense rims (Figures 4b–4d). We distinguish three textural layers in the transitional bombs which are a dense rim (layer A), a transitional zone (layer B), and a vesicular interior (layer C; Figures 4b and 4c). The transitional bombs can further be differentiated into two subclasses, which are (i)

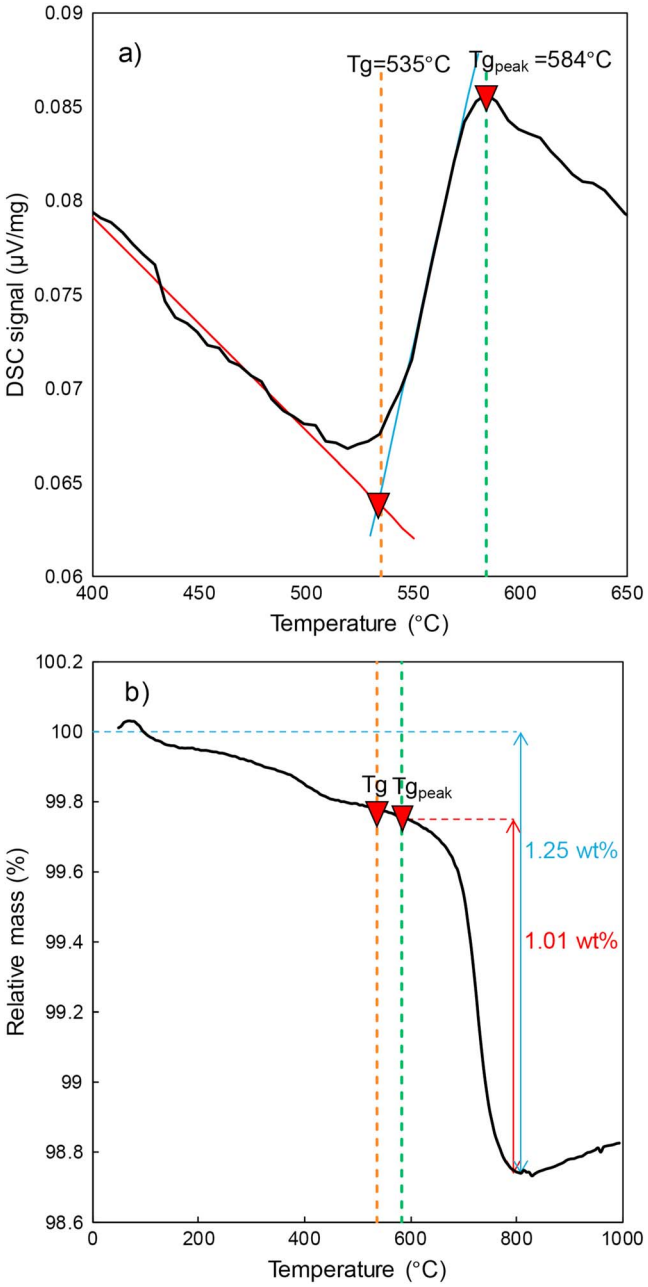

Figure 3. (a) Heat flow signal versus temperature during heating at 10°C/min and estimation of the glass transition temperature T_g. T_g was estimated to onset between 535 and 584°C. (b) Relative mass loss, resulting from degassing of meteoritic and magmatic water initially present in the glass, versus temperature during heating process. The total mass loss is estimated at 1.25 wt.%. The magmatic water was assessed by measuring the mass loss after heating above T_g, providing an estimation of the magmatic water content of about 1.01 wt.%.

bombs with a thick, dense transitional zone that abruptly transitions into more vesicular interior (Type 1; Figure 4b) and (ii) bombs with a gradual increase in vesicularity from the transitional zone toward the core (Type 2; Figure 4c). The core vesicularity is also generally higher in the Type 2 transitional bombs. Type 2 transitional bombs resemble the transitional bombs from Lō'ihi Seamount, Hawai'i for which three textural zones were also defined (Figure 3 in Schipper et al., 2010). Bombs and lapilli show a groundmass with moderate to high microlite content (Figures 4e and 4f).

4.2. VSD and Number Density

First, we note that the vesicularities and vesicle number densities obtained on the same samples in 2-D (SEM) and 3-D (XCT) are generally similar (Table 1). Figure 5 shows the 2-D and 3-D VSD as histograms of the equivalent vesicle diameter L for selected samples. The vesicle diameters measured here span 4 orders of magnitude from 0.004 to $>$1 mm. HH37-3 displays a unimodal distribution in 2-D with L ranging from 0.004 to 0.6 mm and a bimodal distribution in 3-D with a small population (mode A) ranging from 0.01 to 0.3 mm and a large population (mode B) ranging from 0.3 to 0.8 mm. A very similar bimodal distribution is observed in 3-D for the lapillus HH28-3 with the same volume fractions and vesicle sizes for the two modes. The 2-D distribution for a bomb (B74) also shows a bimodal arrangement, but the transition between the small and large populations occurs at 0.05 mm.

4.3. Vesicularity and Vesicle Connectivity

The connectivity versus vesicularity data obtained by pycnometry (C_1) and XCT (C_2) are shown in Figure 6. Figure 6a represents the data obtained by He-pycnometry with a comparison with literature data from basaltic scoria from Hawaiian and Strombolian eruptions and andesitic bread-crust bombs and pumices (compiled in Colombier et al., 2017). Figure 6b shows the data measured by XCT on lapilli and on a profile in a bomb together with XCT literature data on basaltic scoria (Polacci et al., 2008, 2012). Finally, comparisons were made between pycnometry and XCT data (Figure 6c). Volume renderings showing the internal textures of the lapilli and the bomb rim-to-core profile analyzed by XCT are shown in Figure 7.

The measurements of solid density on three lapilli and three bombs yielded ρ_s = 2,843 ± 65 and 2,854 ± 82 kg/m^3, respectively. The vesicularity measured by He-pycnometry ranges from 0.37 to 0.89 in the lapilli and from 0.27 to 0.85 for the bombs (see Table 2). The connectivity C_1 ranges between 0.35 and 0.99 for the lapilli and between 0.45 and 0.99 for the bombs. C_1 increases sharply from 0.35 at a vesicularity of 0.37 to 0.99 at a vesicularity of 0.55 in the lapilli. A similar positive correlation is observed for the bombs with an increase of C_1 from 0.45 to 0.99 at vesicularities between 0.27 and 0.61, but the increase of C_1 with vesicularity seems to occur at a lower vesicularity window. At vesicularities higher than 0.60, both lapilli and bombs have high connectivities ($C_1 > 0.97$). The data for lapilli and bombs display a similar connectivity range as for basaltic scoria from Hawaiian and Strombolian eruptions but within a lower vesicularity window (Colombier et al., 2017). In contrast, they have a significantly broader range of connectivities at a given vesicularity compared to andesitic bread-crust bombs and pumices (Colombier et al., 2017).

The XCT data (Figure 6b) show a range of vesicularities between 0.2 and 0.6 for the lapilli and from 0.3 to 0.85 in the rim-to-core profile in the bomb. The connectivity C_2 covers an entire range from isolated (i.e., C_2 = 0;

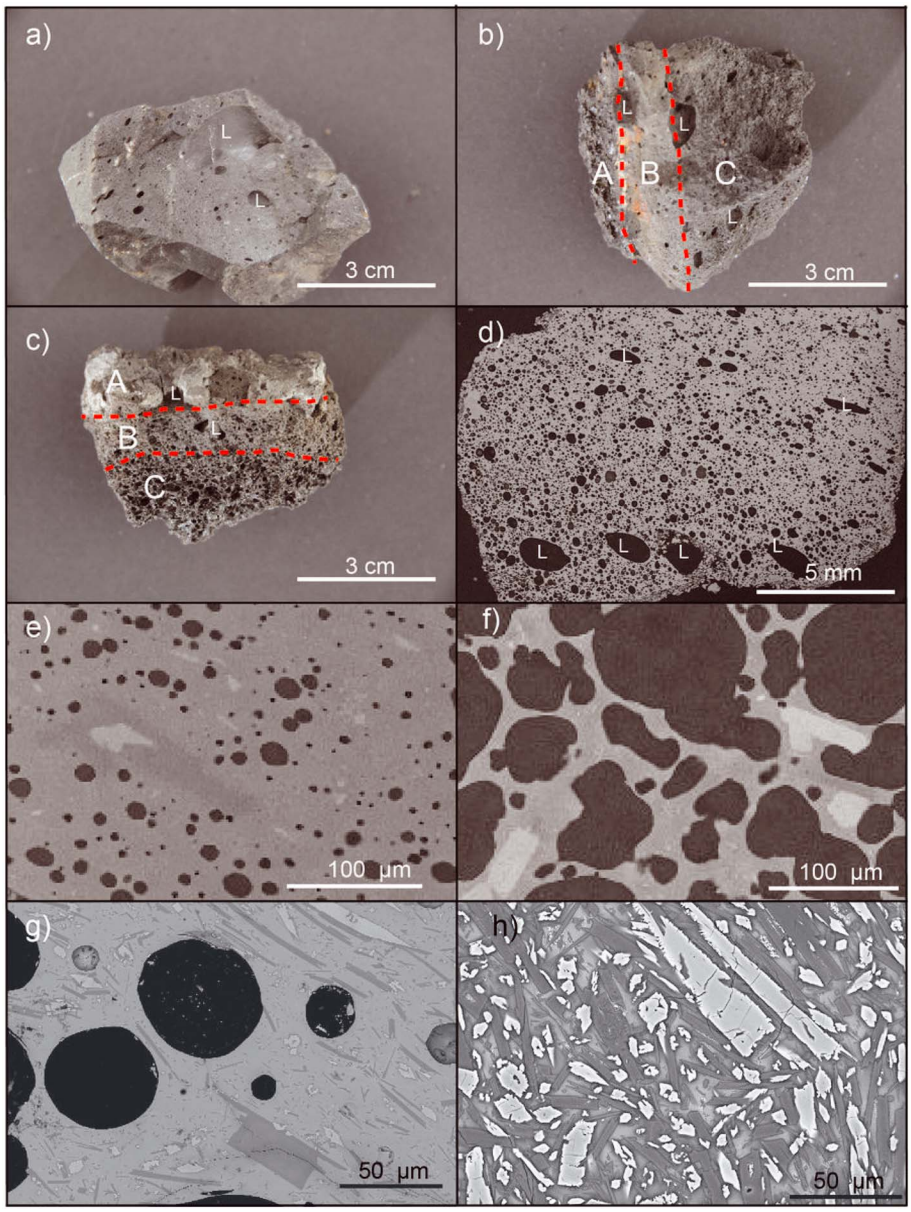

Figure 4. The textural variations in bombs and lapilli. (a) Dense bomb B74 (Φ = 0.25) from the 2009 deposits. (b and c) Transitional bombs with rim to core textural variations. The red dashed lines define the boundaries between the dense rim (layer A), the transitional zone (layer B), and the more vesicular interior (layer C). (b) Type 1 transitional bomb (B30) with abrupt transitions between the three textural layers and moderately vesicular core. (c) Type 2 transitional bomb (B71) also divided in three textural layers but with more gradual textural transitions and a more vesicular interior. (d) SEM image of a transitional lapillus (HH37-3; Φ = 0.38) with textural variations similar to those in the transitional bombs. Note the presence of large vesicles in all specimens (marked with L). (e) XCT image showing a dense lapillus (HH28-3) with mostly isolated vesicles. (f) XCT image showing a vesicular lapillus (HH47-2). (g) Zoom of (d) showing isolated vesicles in a groundmass with moderate microlite content. (h) SEM image of the groundmass of the dense bomb B74 (a) highlighting the high microlite content in this sample. SEM = scanning electron microscopy; XCT = X-ray computed tomography.

Figure 6a) to completely connected (i.e., C_2 = 1; Figures 6d, 6g, and 6h) and increases with vesicularity. All the data from lapilli and the profile in the bomb follow a similar positive trend. The onset of connectivity, which is the percolation threshold Φ_c, occurs at a vesicularity of 0.2. In the dense lapilli with low vesicle connectivity, we see that the onset of percolation is related to the presence of large, elongated vesicles (Figures 7b and 7c). C_2 also increases with Φ from rim to core in the bomb (Figures 6b and 7e–7h). Literature data for scoria from

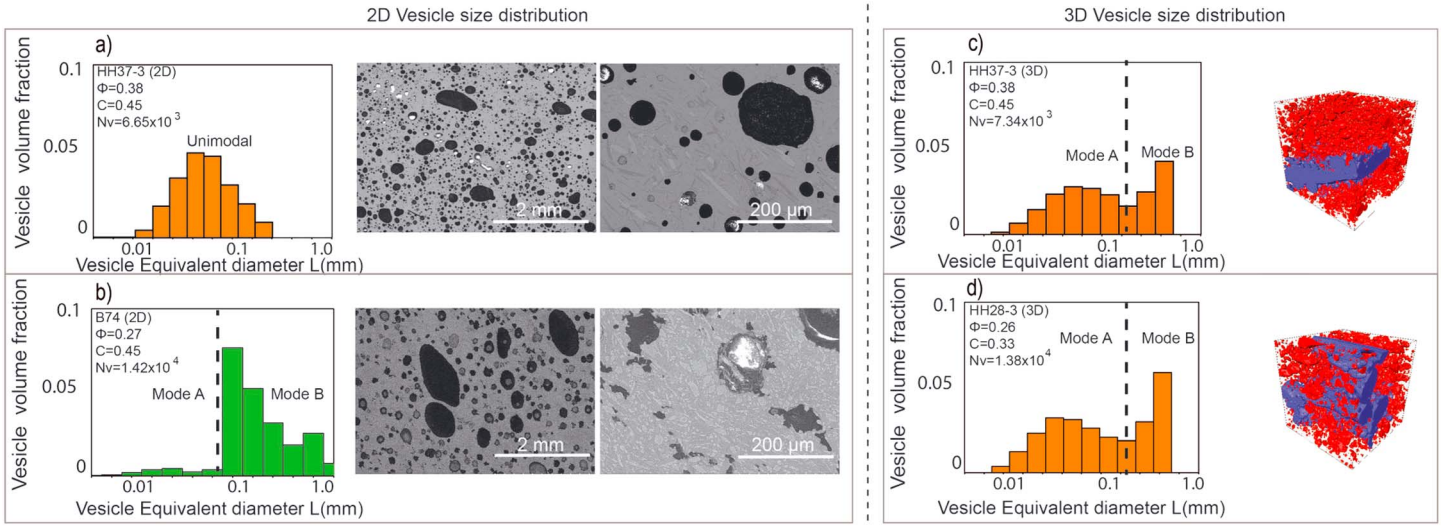

Figure 5. The 2-D and 3-D vesicle size distributions. Size distributions are expressed as vesicle volume fraction versus vesicle equivalent diameter with 2-D data stereologically corrected after Shea et al. (2010); see text for details). backscattered electrons-SEM 2-D data and 3-D renders of the XCT data, with isolated vesicles shown in red and interconnected vesicles in blue, are also shown. Histograms in orange are from lapilli, green from bombs. (a, b) Unimodal VSD for the lapillus HH37-3 in 2-D and compared to bimodal VSD in 3-D data set for the same sample. (c) Bimodal VSD for the bomb B74 in 2-D with more irregular vesicle shapes than in lapillus HH37-3. (d) Bimodal VSD for the lapillus HH28-3. SEM = scanning electron microscopy; XCT = X-ray computed tomography; VSD = vesicle size distribution.

basaltic eruptions show that the connectivity also covers a full range, but within a higher vesicularity window, consistent with the comparison based on pycnometry data (Figure 6a).

Comparison of data measured by both techniques (Figure 6c) demonstrates that the trends are similar with an increase in connectivity with vesicularity. XCT allows us to analyze rocks with very low connectivity and to retrieve the percolation threshold and is therefore complementary to the pycnometry data.

5. Discussion

5.1. Vesiculation and Percolation Threshold

The broad vesicularity range for the lapilli and bombs (Φ between 0.21 and 0.89) from the 2014–2015 eruption is consistent with data obtained from other Surtseyan eruptions (Cole et al., 2001; Jutzeler et al., 2016; Murtagh et al., 2011, 2013).

The connectivity trends observed with vesicularity in volcanic rocks provide insight into the relative degree of bubble nucleation, growth, and coalescence in the parent magma (Colombier et al., 2017). At vesicularities below the percolation threshold, bubble nucleation and growth are dominant; any spatially limited coalescence does not form a connected and permeable network. At the percolation threshold, coalescence starts spanning the system (i.e., the system is percolating) and connectivity increases dramatically with vesicularity until completion ($C = 1$). Connectivity then remains nearly at unity, but vesicularity can still increase dramatically due to further bubble growth and expansion.

In data obtained for vesiculating systems (see Colombier et al., 2017 for a compilation), the majority of scoria and pumice showed a high connectivity and large variability. The variability or scatter makes it difficult to determine a precise percolation threshold, which in any case is likely to vary significantly for vesiculating systems (e.g., Colombier et al., 2017). In this study, we observed (i) that connectivity in lapilli and bombs covered a full range from 0 (fully isolated) to 1 (fully connected) and (ii) that there is a clear and strong increase of connectivity with vesicularity. The C versus Φ trends obtained by XCT for the lapilli and bombs suggest a low percolation threshold of $\Phi_c \approx 0.20$. This is lower than values reported for basaltic scoria from Hawaiian and Strombolian eruptions (Figures 6a and 6b). The percolation threshold is dependent on several parameters, such as melt crystallinity and surface tension (Blower, 2001), bubble shape (e.g., Okumura et al., 2008), pore geometry (cracks/vesicles) (Colombier et al., 2017; Mueller et al., 2005), and bubble size distribution (e.g., Burgisser et al., 2017). Here we examine what may have caused the apparent low percolation threshold seen in our Tongan samples.

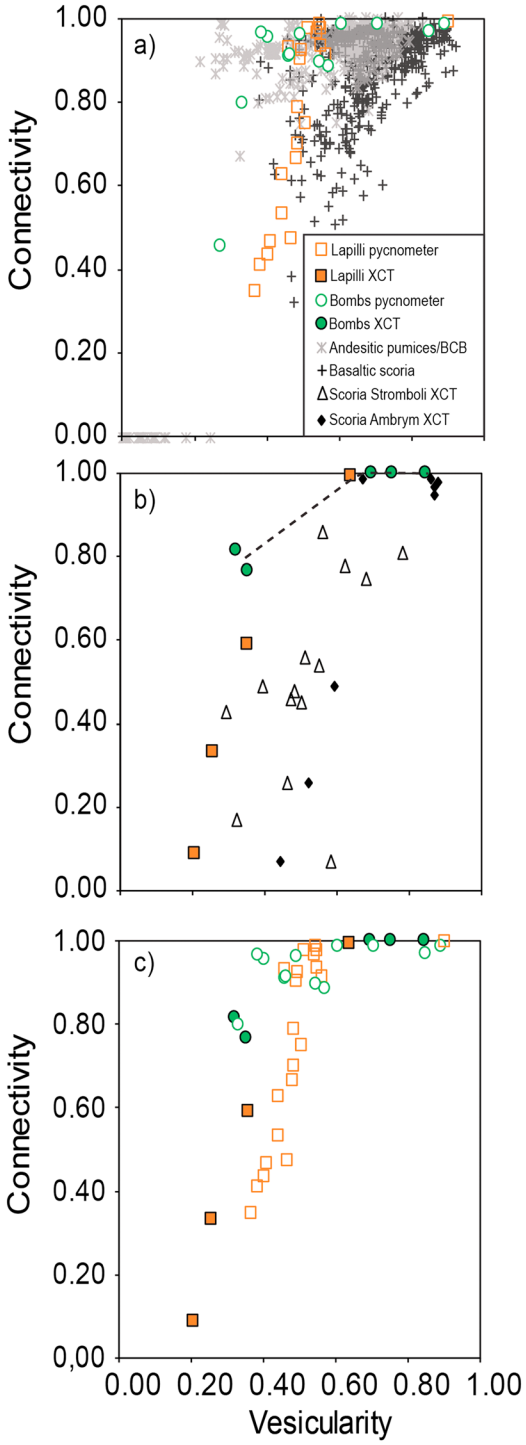

Figure 6. Connectivity-vesicularity relationships for the lapilli and bombs and comparison with other natural volcanic rocks. (a) C_1 versus Φ measured by Helium pycnometry: Lapilli and bombs from this study, andesitic pumices, and bread-crust bombs and basaltic scoria (Colombier et al., 2017). (b) C_2 versus Φ as measured by XCT: lapilli, rim-to-core profile in a bomb (dashed line), basaltic scoria from Stromboli volcano (Polacci et al., 2008), and Ambrym volcano (Polacci et al., 2012). The XCT data can also be used to calculate C1 connectivity if required. (c) Comparison of the He pycnometry and XCT data showing good agreement between the *C* and Φ trends. XCT = X-ray computed tomography.

The VSD in these samples is highly polydisperse and bimodal (Figure 5), which should favor a higher percolation threshold in the case of crystal-free melts with spherical bubbles (Blower, 2001). However, in some samples we observed that large, elongated vesicles led to percolation and onset of connectivity, highlighting the influence of deformation on the percolation threshold (Figures 7b and 7c). Garboczi et al. (1995) showed with numerical simulations that increasing the elongation of overlapping ellipsoids led to a reduction of the percolation threshold from 0.28 for spheres to about 0.20 for ellipsoids with aspect ratios of 3 to 4. This is consistent with the percolation threshold found in this study and with the elongation of the large interconnected vesicles. A low percolation threshold can also be explained by the moderate to high melt crystallinity observed in the lapilli and bombs (Figures 4g and 4h). Crystals enhance bubble connectivity at a given vesicularity, by reducing the space between bubbles and by inducing bubble deformation and migration (Blower, 2001; Lindoo et al., 2017; Oppenheimer et al., 2015). We propose that the low percolation threshold observed here is the result of a complex interplay between bubble deformation and high crystal content (both tend to reduce the percolation threshold) on the one hand and polydispersivity (promoting a higher percolation threshold instead) on the other hand.

5.2. Origin of the Textural Variations in the Lapilli and Bombs

The broad range of connectivities and low average values observed in the lapilli and bombs contrast with the more common high connectivities typically observed in other volcanic rocks (Colombier et al., 2017). For fire-fountaining activity or bread-crust bombs from Vulcanian eruptions Colombier et al. (2017) proposed that low average but broad ranges in connectivity may reflect quenching hindering postfragmentation vesiculation. The gradual textural variations observed in the Tongan transitional, rim-to-core profiles are similar to those seen in scoria from fire-fountaining eruptions (e.g., Stovall et al., 2011), bread-crust bombs from Vulcanian eruptions (Giachetti et al., 2010; H. M. N. Wright et al., 2007), or pyroclasts from shallow or deep subaqueous eruptions (e.g., Jutzeler et al., 2016; Schipper et al., 2010). The rims in such specimens preserve low vesicularity and small, isolated vesicles, inferred to represent the state of the magma at the point of fragmentation. In contrast, the cores show large, completely coalesced (connected) vesicles that are interpreted as the result of extensive bubble growth and coalescence occurring after fragmentation (Stovall et al., 2011). We therefore propose that the transitional lapilli and bombs from the 2009 and 2014–2015 eruption and the associated *C* versus Φ trends were the result of postfragmentation vesiculation. As the dense, transitional and vesicular lapilli and bombs follow a similar *C* versus Φ path, all the textures appear to reflect different degrees of vesiculation that were interrupted by quenching by contact with water. Hence, dense particles and dense margins of transitional particles had less time for vesiculation, whereas vesicular clasts and cores of transitional particles were insulated enough for bubbles to continue growing, leading to an increase of connectivity and vesicularity. Variations of the timing of quenching by water and vesiculation could be due to clast size and initial melt temperature, along with the radial distance of the melt to the coolant in the case of transitional clasts or

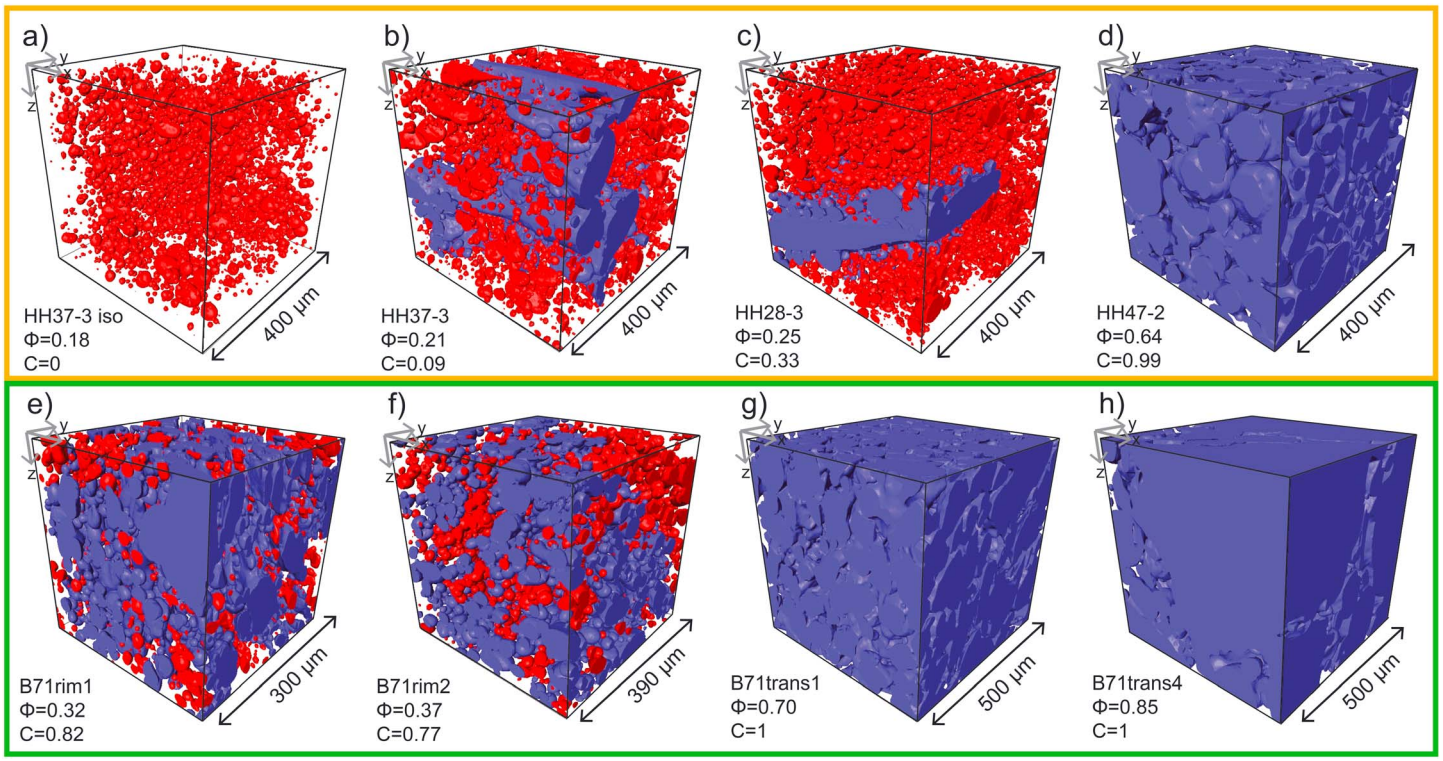

Figure 7. Volume renderings of XCT data. Top row (orange) lapilli. Bottom row (green) a radial profile through a bomb. Vesicles connected in the *x* direction are shown in blue and nonconnected vesicles in red. (a–d) The variability within the lapilli, from only isolated vesicles (a) through mostly isolated vesicles with a few large and elongated vesicles (b and c) allowing flow in the *x* direction to be fully connected (d). The profile through bomb B71 (Figure 4e) shows an increase in connectivity, vesicularity and vesicle volume from rim (e and f) to core (g and h). XCT = X-ray computed tomography.

the presence of an insulating vapor film that would allow longer vesiculation until film collapse and quenching. In the following section, we explore these processes.

5.3. Vesicle Size Distribution

The vesicle number densities of the Tongan lapilli and bombs (Table 1) have values typical of shallow subaqueous mafic eruptions (Jutzeler et al., 2016), and the values are similar using either 2-D or 3-D methods for sample HH37-3 (Table 1). However, there are discrepancies in the VSD in 2-D and 3-D measurements. For the same lapillus HH37-3, the VSD is unimodal in 2-D and bimodal in 3-D (Figures 5a and 5c). This reflects the presence of a significant population of elongated vesicles in the dense particles, also observed visually in the most dense lapilli and bombs (Figures 4 and 7). This population is missed in 2-D analysis because the large vesicles were not intersected along their long axis during thin-section preparation. This highlights the importance of using 3-D techniques for anisotropic textures that are not easily converted from 2-D images by stereological techniques.

The population of large vesicles (mode B; Figure 5) is present in both dense and vesicular parts of the transitional lapilli and bombs. Since the dense rims were formed by water quenching, the large vesicles must have predated contact with water and were likely present at the time of fragmentation. Thus, mode B is the result of bubble nucleation and growth during magma ascent in the conduit. In turn, the small vesicles (mode A; Figure 5) increase significantly in size from rim to core, therefore reflecting postfragmentation vesiculation interrupted at different stages by quenching.

6. Cooling Processes During the 2014–2015 Eruption

6.1. Direct Magma-Water Contact or Leidenfrost Effect?

The cooling of melt droplets in water depends on the presence or absence of a stable vapor film at the magma-water interface (film boiling or Leidenfrost effect; Schipper et al., 2013). For direct magma-water contact, cooling occurs dominantly by conductive heat transfer in the particle toward the rim, which is rapidly

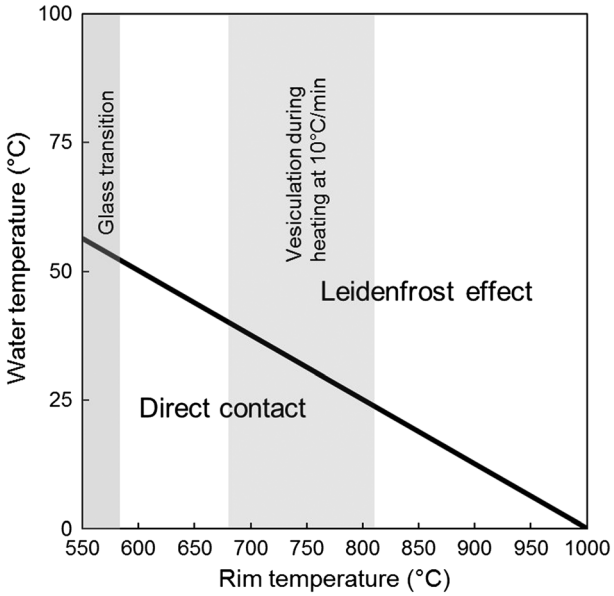

Figure 8. Diagram showing the water and rim temperature conditions for direct magma-water contact and the formation of a stable vapor film (Leidenfrost effect; after Dhir & Puhorit, 1978), the glass transition temperature range, and the vesiculation range as determined from the thermal analysis (see text for details, Figure 3).

quenched to the ambient value (Mastin, 2007). An insulating film may reduce the rate of heat transfer by up to 2 orders of magnitude (Schipper et al., 2013), and cooling in the Leidenfrost case occurs by conduction, convection, and radiation (e.g., van Otterloo et al., 2015). The Leidenfrost temperature T_L corresponds to the minimum melt temperature required to maintain a stable vapor film and depends on the degree of undercooling (i.e., the difference between the boiling point T_b and the surrounding water temperature T_w). It can be estimated by (Dhir & Puhorit, 1978)

$$T_L = 201 + 8(T_b - T_w) \quad (5)$$

We assume that T_w can vary spatially and temporally between ambient (~25°C) and boiling (100°C) water temperature in a Surtseyan plume yielding T_L values between 201 and 801°C.

Using equation (5), we can estimate the conditions under which direct contact or the Leidenfrost effect dominates (Figure 8). We assume that the melt temperature at the rim varies between the initial (T_{mi} = 1000°C) and T_g (545°C) due to cooling. Under this range of conditions, both Leidenfrost effect and direct contact are possible during cooling (Figure 8). We will thus consider both the pure conduction (direct contact) case and Leidenfrost case which approximately correspond to cases (1) and (2) discussed in methodology.

6.2. Thermal Modeling

We calculated the time available for vesiculation in the core of melt particles under both pure conduction and Leidenfrost effect cases, that is, the time t required for the core to cool to the glass transition temperature T_g (quenching), as a function of particle radius R. The results for particles of two vesicularities (0.2 and 0.6) and an initial melt temperature of 1000°C are shown in Figure 9.

The time spent above T_g of a particle before quenching to T_g is dominantly influenced by the particle radius. For the smallest particles (R = 5 mm), the time required for the core to reach T_g is between 6 and 28 s, whereas it takes more than 17.5 hr for the core of the largest particles (R = 500 mm). At a given particle radius, we also observe the influence of vesicularity and of the Leidenfrost effect. For large particle radius (typically R > 100 mm), vesicularity has a greater influence than the Leidenfrost effect on the cooling time of the core. Increasing vesicularity increases the time required to quench a particle. In contrast, the Leidenfrost effect becomes more important as particle size decreases and the time for vesiculation logically increases in the presence of a stable vapor film. A power law describes the relationship in the pure conduction case.

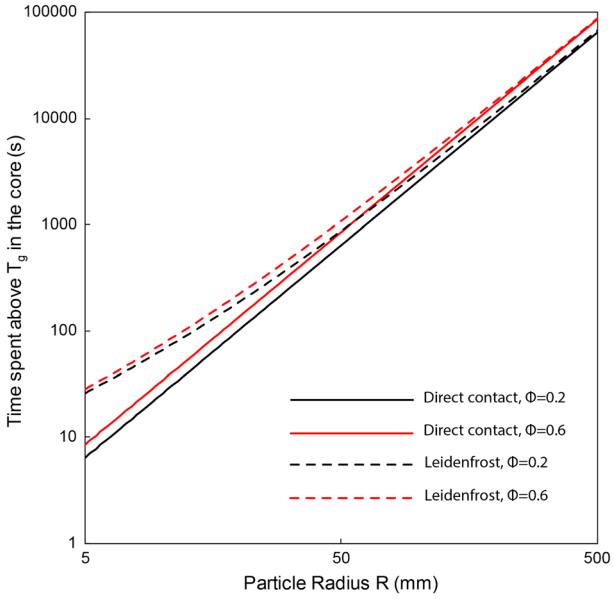

Figure 9. Relationship between time before quenching below T_g in the core and particle radius for both direct contact and Leidenfrost effect at a vesicularity of 0.2 and 0.6.

We also computed the evolution of the temperature from rim to core in particles of different sizes and vesicularities for the two contact cases (Figure 10). In the case of pure conduction, the particle rims reach T_g instantaneously, whereas in the Leidenfrost case the cooling at the rim is delayed by heat transfer to the vapor film. At a given radius and radial distance from the rim, the effect of vesicularity is minor. In the case of conduction only, the temperature at the outer rim of the particles drops to T_g and the time available for vesiculation is small (Figure 10a). The smaller the particle, the faster the region close to the rim is quenched and the less time available for vesiculation. Rim quenching is significantly slower in the presence of a stable vapor film (Figure 10b). Core quenching is in turn only slightly slower than in the

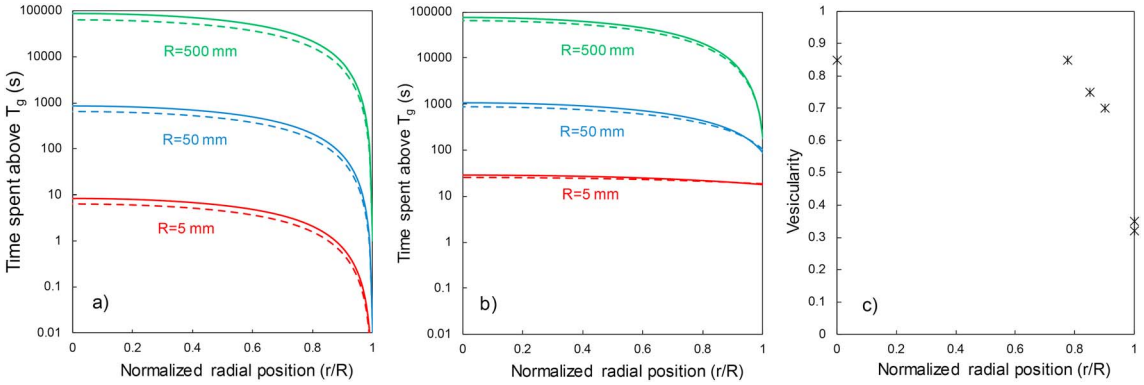

Figure 10. Relationship between the time before quenching below T_g and radial position for spherical melt droplets of different radius for direct contact (a) and Leidenfrost (b) cooling. Particles radius R = 5 mm (red), R = 50 mm (blue), and R = 500 mm (green), with a vesicularity of 0.2 (dashed) and 0.6 (solid). (c) The relationship of vesicularity (3-D) with normalized radial position in the transitional bomb B71 (Figure 4e), radius of 50 mm. Note that values of r/R equal to 0 and 1 correspond to particle cores and rims, respectively.

direct contact case (Figure 10b). For the smallest particles (R = 5 mm), the gradient of time spent above T_g between rim and core is small in the Leidenfrost case (Figure 10b). One bomb (B71; see Figure 4c) shows a similar vesicularity profile as the computed gradient of time spent above T_g at intermediate times

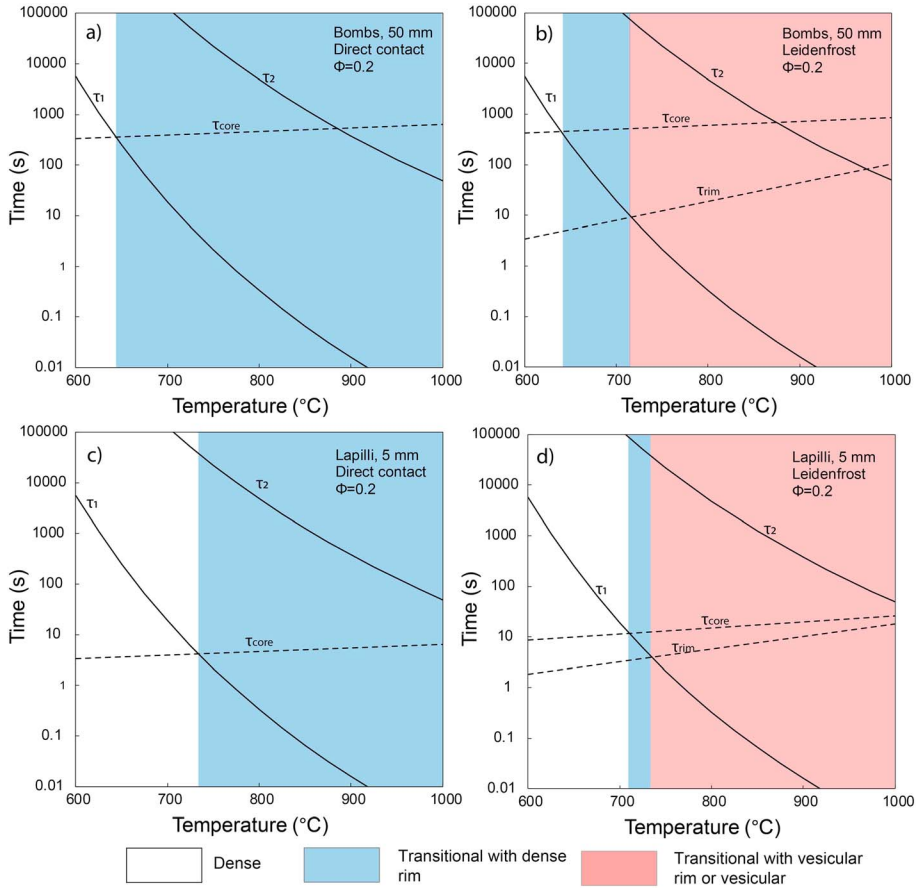

Figure 11. Evolution of the timescales of vesiculation by expansion (τ_1), diffusion (τ_2), cooling at the rim (τ_{rim}), and at the core (τ_{core}) of the bombs (a, b) and lapili (c, d) as a function of temperature for the direct contact and Leidenfrost cases and for a starting vesicularity of 0.2. The temperature ranges at which dense, transitional, and vesicular textures are likely preserved are illustrated. In the direct contact case, τ_{rim} = 0 due to the thermal modeling condition in which the surface temperature is instantaneously dropped to the water temperature and is therefore not illustrated in (a) and (c).

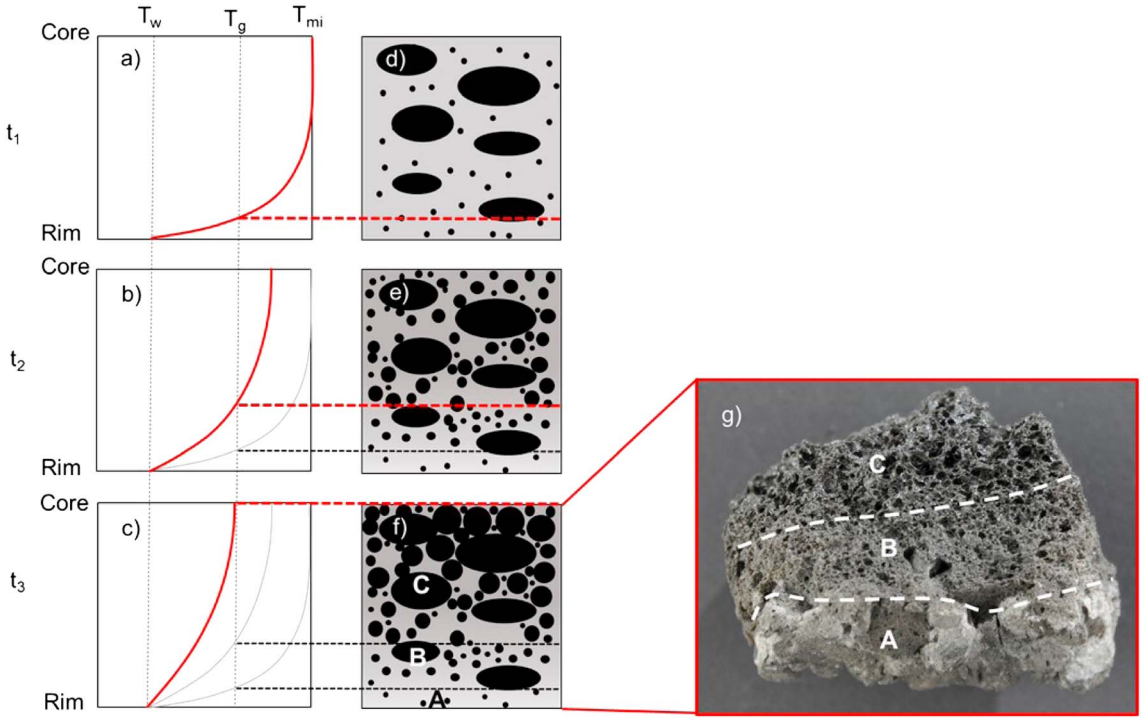

Figure 12. Conceptual model showing relationship between temperature (left panel, a–c) and vesiculation (middle panel, d–f) during cooling from time t_1 to time t_3 and explaining the formation of transitional textures. The red line shows the core-rim temperature profiles during cooling from a high initial melt temperature ($T_{mi} >> T_g$), and the red dashed lines (d–f) represent the location of the T_g isotherm in the sample (black dashed lines in (e) and (f) show former position of the isotherm); below this line the sample cannot undergo further vesiculation. (g) Transitional texture preserved at t_3. White dashed lines show boundaries between textural zones A to C (dense rim, transitional zone, and vesicular core; see text for details).

(Figure 10c), suggesting that the time available for vesiculation before cooling could be the dominant factor responsible for the observed gradual textural variations in bombs and lapilli.

6.3. Link Between Cooling and Vesiculation

Here we consider simple timescales of cooling and vesiculation during magma-water interaction in order to link the textural features of the pyroclasts to the cooling processes. Postfragmentation vesiculation is governed by an expansion timescale related to decompression $\tau_1=(1-\Phi)3\eta/(4P)$ (Barclay et al., 1995) and a diffusion timescale $\tau_2=R^2/D$, where η is the viscosity, P is the pressure external to the bubbles (hydrostatic in our case), R is the bubble radius, and D the diffusivity of the melt. η was estimated for a range of temperature from 600 to 1000°C using the model of Giordano et al. (2008) to be $3.94 \times 10^3 < \eta < 1.47 \times 10^{10}$ Pa s. P was calculated to be 1.57×10^6 Pa considering a water depth of 150 m based on the depth of the caldera basin although a shallower depth is not excluded during the emergent phase of the 2014–2015 eruption. The smallest vesicle size observed in the VSD (R = 2 μm) was chosen for the bubble radius. Finally, D was retrieved using the model of Zhang and Ni (2010) for andesitic composition melts and has the range $3.98 \times 10^{-19} < D < 8.14 \times 10^{-14}$ m^2/s. We compare these vesiculation timescales to the cooling timescales at the rims τ_{rim} and cores τ_{core} of lapilli (5 mm) and bombs (50 mm) for a range of temperature between 600 and 1000°C (Figures 11a–11d). Both direct contact and Leidenfrost case are considered.

τ_1 is several orders of magnitude smaller than τ_2 at any temperature, and therefore, expansion is the dominant process during postfragmentation vesiculation of the lapilli and bombs (Figure 11). If $\tau_1 > \tau_{core} > \tau_{rim}$, the entire clast can cool before the onset of vesiculation and preserves a dense texture (Figure 11). If $\tau_{core} > \tau_1 > \tau_{rim}$, the rim quenches before vesiculating but vesiculation can occur in the core. The clast can preserve a transitional texture if the vesiculation is fast in the core (Figure 11). Finally, in the Leidenfrost case, if $\tau_{core} > \tau_{rim} > \tau_1$, the whole particle can vesiculate (Figures 11b and 11d). However, the time for vesiculation is higher in the core than in the rim, leading to a transitional texture. The cooling time for lapilli

rim and core converges at high temperature (Figures 10b and 11d). This will promote preservation of more homogeneous vesicular clasts. These observations are in agreement with the dominance of dense and transitional lapilli and bombs, with only a small number of vesicular lapilli. This model suggests that bombs require an initial melt temperature lower than ~650°C to preserve a dense texture. Although vesiculation by diffusion is slower than expansion, it can also occur in the bombs at high temperatures.

We propose a conceptual model that explains the gradual textural variations observed in the transitional lapilli and bombs with the temporal evolution of temperature (Figures 12a–12c) and vesiculation (Figures 12d–12f). In this model, the initial melt temperature is highly above T_g (red curve in Figure 12a). At time t_1, the particle contains preexisting large bubbles with low vesicularity and a second bubble nucleation event starts (Figure 12d). The particle rim drops rapidly below T_g leading to solidification and arrest of the textural evolution in the rim. Vesiculation continues in the interior. At time t_2, a transitional zone of the particle between the rim and the core is now also cooled below T_g (Figures 12b and 12e). Vesiculation continues in the core of the particle. At time t_3, the whole particle is cooled below T_g and a final, transitional texture is preserved (Figures 12c and 12f).

7. Conclusion

The textures of pyroclasts from the Hunga Tonga-Hunga Ha'apai volcano—erupted in 2009 and 2014–2015—preserve textural clues to the conditions of their formation. We have combined 2-D and 3-D vesicle analyses to constrain bulk vesicularity and vesicle metrics from rim to core in bombs and lapilli of a range of sizes. We additionally ran a numerical thermal model that resulted in a conceptual and a quantitative view of the cooling trajectory of these same particles. We conclude that the particle size, the Leidenfrost effect, and initial temperature are the dominant factors in explaining how these particles continued to vesiculate postfragmentation. A combination of textural and numerical constraints is the key to understanding submarine and emergent eruptions that are difficult to characterize in situ during the event. Conditions of cooling in a Surtseyan eruption are an interesting test bed, because they display a variety of cooling/quenching conditions that influence the intensity of thermal stress experienced by glassy particles and the subsequent quench-induced fragmentation. This, in turn, influences the amount of fine ash in Surtseyan plumes—which is a notable aviation hazard. For this reason, further work should experimentally focus on the link between cooling and secondary fragmentation processes in conditions relevant to Surtseyan settings. Geospeedometry measurements on glassy particles of different size from Surtseyan eruptions could be additionally used to test the results of our thermal modeling and explore the role of particle size and vesicularity on cooling, as well as track the evolution of cooling rates during progressive emergence of tuff cones.

This study has also provided new insights into the percolation threshold and the effect of shear deformation, crystallinity, and VSD on this threshold. X-ray microcomputed tomography was shown to be a very effective addition to pycnometry measurements of connectivity, especially in the case of rocks with low connectivity, and therefore close to the percolation threshold. In situ vesiculation experiments combined with systematic assessment of connectivity and vesicularity could allow us to track the percolation threshold in vesiculating magmas with different properties and to understand the factors controlling this threshold, which is of paramount importance to better understand the onset of outgassing in volcanic conduits.

Acknowledgments

S. J. C., M. B., and M. T. thank the Faculty of Science Development Research Fund, the *Pacific Rose* crew from Pacific Sunrise Fishing, and the Geology Unit of the Tongan Ministry of Lands and Natural Resources for supporting the collection of samples used in this work. M. C. and D. B. D. acknowledge support from an ERC Advanced Grant (Explosive Volcanism in the Earth System: EVOKES - 247076) to D. B. D. K. J. D. was supported by EVOKES and NERC grant NE/M018687/1. We thank Michael Walter for editorial handling of the manuscript. This paper has benefited from constructive reviews by Karen Fontijn and an anonymous reviewer. All raw and processed data not tabulated in the article are available in the supporting information.

References

Bagdassarov, N., & Dingwell, D. (1994). Thermal properties of vesicular rhyolite. *Journal of Volcanology and Geothermal Research*, *60*(2), 179–191. https://doi.org/10.1016/0377-0273(94)90067-1

Bai, L., Baker, D. R., & Hill, R. J. (2010). Permeability of vesicular Stromboli basaltic glass: Lattice Boltzmann simulations and laboratory measurements. *Journal of Geophysical Research*, *115*, B07201. https://doi.org/10.1029/2009JB007047

Barclay, J., Riley, D. S., & Sparks, R. S. J. (1995). Analytical models for bubble growth during decompression of high viscosity magmas. *Bulletin of Volcanology*, *57*(6), 422–431. https://doi.org/10.1007/BF00300986

Blower, J. (2001). Factors controlling permeability-porosity relationships in magma. *Bulletin of Volcanology*, *63*(7), 497–504. https://doi.org/10.1007/s004450100172

Bohnenstiehl, D. R., Dziak, R. P., Matsumoto, H., & Lau, T. K. A. (2013). Underwater acoustic records from the March 2009 eruption of Hunga Ha'apai-Hunga Tonga volcano in the Kingdom of Tonga. *Journal of Volcanology and Geothermal Research*, *249*, 12–24. https://doi.org/10.1016/j.jvolgeores.2012.08.014

Bryan, S. E., Cook, A., Evans, J. P., Colls, P. W., Wells, M. G., Lawrence, M. G., et al. (2004). Pumice rafting and faunal dispersion during 2001–2002 in the Southwest Pacific: Record of a dacitic submarine explosive eruption from Tonga. *Earth and Planetary Science Letters*, *227*(1-2), 135–154. https://doi.org/10.1016/j.epsl.2004.08.009

Bryan, W. B., Stice, G. D., & Ewart, A. (1972). Geology, and geochemistry of the volcanic islands of Tonga. *Journal of Geophysical Research*, *77*(8), 1566–1585. https://doi.org/10.1029/JB077i008p01566

Buades, A., Coll, B., & Morel, J. (2011). Non-local means denoising pixelwise implementation. *Image Processing Line*, *1*, 208–212. https://doi.org/10.5201/ipol.2011.bcm_nlm

Burgisser, A., Chevalier, L., Gardner, J. E., & Castro, J. M. (2017). The percolation threshold and permeability evolution of ascending magmas. *Earth and Planetary Science Letters*, *470*, 37–47. https://doi.org/10.1016/j.epsl.2017.04.023

Cole, P., Guest, J., Duncan, A., & Pacheco, J. (2001). Capelinhos 1957-1958, Faial, Azores: Deposits formed by an emergent surtseyan eruption. *Bulletin of Volcanology*, *63*(2-3), 204–220. https://doi.org/10.1007/s004450100136

Colombier, M., Wadsworth, F. B., Gurioli, L., Scheu, B., Kueppers, U., Di Muro, A., & Dingwell, D. B. (2017). The evolution of pore connectivity in volcanic rocks. *Earth and Planetary Science Letters*, *462*, 99–109. https://doi.org/10.1016/j.epsl.2017.01.011

Connor, C. B., Lichtner, P. C., Conway, F. M., Hill, B. E., Ovsyannikov, A. A., Federchenko, I., et al. (1997). Cooling of an igneous dike 20 yr after intrusion. *Geology*, *25*(8), 711–714. https://doi.org/10.1130/0091-7613(1997)025%3C0711:COAIDY%3E2.3.CO;2

Couves, C., Roberts, S., Racey, A., Troth, I., & Best, A. (2016). Use of X-ray computed tomography to quantify the petrophysical properties of volcanic rocks: A case study from Tenerife, Canary Islands. *Journal of Petroleum Geology*, *39*(1), 79–94. https://doi.org/10.1111/jpg.12629

Crank, J. (1975). Diffusion in a plane sheet. *The mathematics of diffusion*, *2*, 44–68.

Dhir, V. K., & Puhorit, G. P. (1978). Subcooled film-boiling heat transfer from spheres. *Nuclear Engineering and Design*, *47*(1), 49–66. https://doi.org/10.1016/0029-5493(78)90004-3

Ewart, A., Collerson, K. D., Regelous, M., Wendt, J. I., & Niu, Y. (1998). Geochemical evolution within the Tonga – Kermadec – Lau Arc – Back-arc Systems: The role of varying mantle wedge composition in space and time. *Journal of Petrology*, *39*(3), 331–368. https://doi.org/10.1093/petroj/39.3.331

Garboczi, E. J., Snyder, K. A., Douglas, J. F., & Thorpe, M. F. (1995). Geometrical percolation threshold of overlapping ellipsoids. *Physics Review*, *52*, 819–828.

Giachetti, T., Druitt, T. H., Burgisser, A., Arbaret, L., & Galven, C. (2010). Bubble nucleation, growth and coalescence during the 1997 Vulcanian explosions of Soufrière Hills Volcano, Montserrat. *Journal of Volcanology and Geothermal Research*, *193*(3-4), 215–231. https://doi.org/10.1016/j.jvolgeores.2010.04.001

Giordano, D., Russell, J. K., & Dingwell, D. B. (2008). Viscosity of magmatic liquids: A model. *Earth and Planetary Science Letters*, *271*(1-4), 123–134. https://doi.org/10.1016/j.epsl.2008.03.038

Global Volcanism Program (1988). Report on Hunga Tonga-Hunga Ha'apai (Tonga). In L. McClelland (Ed.), *Scientific Event Alert Network Bulletin, 13:5*. Smithsonian Institution. https://doi.org/10.5479/si.GVP.SEAN198805-243040

Global Volcanism Program (2009a). Report on Hunga Tonga-Hunga Ha'apai (Tonga). In R. Wunderman (Ed.), *Bulletin of the Global Volcanism Network, 34:2*. Smithsonian Institution. https://doi.org/10.5479/si.GVP.BGVN200902-243040

Global Volcanism Program (2009b). Report on Hunga Tonga-Hunga Ha'apai (Tonga). In R. Wunderman (Ed.), *Bulletin of the Global Volcanism Network, 34:3*. Smithsonian Institution. https://doi.org/10.5479/si.GVP.BGVN200903-243040

Global Volcanism Program (2015). Report on Hunga Tonga-Hunga Ha'apai (Tonga). In R. Wunderman (Ed.), *Bulletin of the Global Volcanism Network, 40:1*. Smithsonian Institution.

Gonnermann, H. M., & Gardner, J. E. (2013). Homogeneous bubble nucleation in rhyolitic melt: Experiments and nonclassical theory. *Geochemistry, Geophysics, Geosystems*, *14*, 4758–4773. https://doi.org/10.1002/ggge.20281

Jutzeler, M., White, J. D. L., Proussevitch, A. A., & Gordee, S. M. (2016). Vesiculation and fragmentation history in a submarine scoria cone-forming eruption, an example from Nishiizu (Izu Peninsula, Japan). *Bulletin of Volcanology*, *78*(2). https://doi.org/10.1007/s00445-016-0999-2

Kokelaar, P. (1986). Magma-water interactions in subaqueous and emergent basaltic volcanism. *Bulletin of Volcanology*, *1*, 275–289.

Kueppers, U., Nichols, A. R. L., Zanon, V., Potuzak, M., & Pacheco, J. M. R. (2012). Lava balloons—Peculiar products of basaltic submarine eruptions. *Bulletin of Volcanology*, *74*(6), 1379–1393. https://doi.org/10.1007/s00445-012-0597-x

Kushnir, A. R. L., Martel, C., Champallier, R., & Arbaret, L. (2017). In situ confirmation of permeability development in shearing bubble-bearing melts and implications for volcanic outgassing bubble-bearing melts and implications for volcanic outgassing. *Earth and Planetary Science Letters*, *458*, 315–326. https://doi.org/10.1016/j.epsl.2016.10.053

Lavallée, Y., Dingwell, D. B., Johnson, J. B., Cimarelli, C., Hornby, A. J., Kendrick, J. E., et al. (2015). Thermal vesiculation during volcanic eruptions. *Nature*, *528*(7583), 544–547. https://doi.org/10.1038/nature16153

Lindoo, A., Larsen, J. F., Cashman, K. V., & Oppenheimer, J. (2017). Crystal controls on permeability development and degassing in basaltic andesite magma. *Geological Society of America*, *45*(9), 831–834. https://doi.org/10.1130/G39157.1

Liu, Y., Zhang, Y., & Behrens, H. (2005). Solubility of H_2O in rhyolitic melts at low pressures and a new empirical model for mixed H_2O – CO_2 solubility in rhyolitic melts. *Journal of Volcanology and Geothermal Research*, *143*(1-3), 219–235. https://doi.org/10.1016/j.jvolgeores.2004.09.019

Mastin, L. G. (2007). Generation of fine hydromagmatic ash by growth and disintegration of glassy rinds. *Journal of Geophysical Research*, *112*, B02203. https://doi.org/10.1029/2005JB003883

Mueller, S., Melnik, O., Spieler, O., Scheu, B., & Dingwell, D. B. (2005). Permeability and degassing of dome lavas undergoing rapid decompression: An experimental determination. *Bulletin of Volcanology*, *67*(6), 526–538. https://doi.org/10.1007/s00445-004-0392-4

Murtagh, R. M., & White, J. D. L. (2013). Pyroclast characteristics of a subaqueous to emergent Surtseyan eruption, Black Point volcano, California. *Journal of Volcanology and Geothermal Research*, *267*, 75–91. https://doi.org/10.1016/j.jvolgeores.2013.08.015

Murtagh, R. M., White, J. D. L., & Kwan, Y. (2011). Pyroclast textures of the Ilchulbong " wet " tuff cone, Jeju Island, South Korea. *Journal of Volcanology and Geothermal Research*, *201*(1-4), 385–396. https://doi.org/10.1016/j.jvolgeores.2010.09.009

Nguyen, C. T., Gonnermann, H. M., Chen, Y., Huber, C., Maiorano, A. A., Gouldstone, A., & Dufek, J. (2013). Film drainage and the lifetime of bubbles. *Geochemistry, Geophysics, Geosystems*, *14*(9), 3616–3631. https://doi.org/10.1002/ggge.20198

Nichols, A. R. L., Potuzak, M., & Dingwell, D. B. (2009). Cooling rates of basaltic hyaloclastites and pillow lava glasses from the HSDP2 drill core. *Geochimica et Cosmochimica Acta*, *73*(4), 1052–1066. https://doi.org/10.1016/j.gca.2008.11.023

Okumura, S., Nakamura, M., Tsuchiyama, A., Nakano, T., & Uesugi, K. (2008). Evolution of bubble microstructure in sheared rhyolite: Formation of a channel-like bubble network. *Journal of Geophysical Research*, *113*, B07208. https://doi.org/10.1029/2007JB005362

Oppenheimer, J., Rust, A. C., Cashman, K. V., & Sandnes, B. (2015). Gas migration regimes and outgassing in particle-rich suspensions. *Frontiers in Physics*, *3*, 60.

Polacci, M., Baker, D. R., Bai, L., & Mancini, L. (2008). Large vesicles record pathways of degassing at basaltic volcanoes. *Bulletin of Volcanology*, *70*(9), 1023–1029. https://doi.org/10.1007/s00445-007-0184-8

Polacci, M., Baker, D. R., La Rue, A., Mancini, L., & Allard, P. (2012). Degassing behaviour of vesiculated basaltic magmas: An example from Ambrym volcano, Vanuatu Arc. *Journal of Volcanology and Geothermal Research*, *233-234*, 55–64. https://doi.org/10.1016/j.jvolgeores.2012.04.019

Potuzak, M., Nichols, A. R. L., Dingwell, D. B., & Clague, D. A. (2008). Hyperquenched volcanic glass from Loihi seamount, Hawaii. *Earth and Planetary Science Letters*, *270*(1-2), 54–62. https://doi.org/10.1016/j.epsl.2008.03.018

Proussevitch, A. A., & Sahagian, D. L. (1998). Dynamics and energetics of bubble growth in magmas: Analytical formulation and numerical modeling Pg. *Journal of Geophysical Research*, *103*(B8), 18,223–18,251. https://doi.org/10.1029/98JB00906

Schipper, C. I., Sonder, I., Schmid, A., White, J. D. L., Dürig, T., Zimanowski, B., & Büttner, R. (2013). Vapour dynamics during magma-water interaction experiments: Hydromagmatic origins of submarine volcaniclastic particles (limu o Pele). *Geophysical Journal International*, *192*(3), 1109–1115. https://doi.org/10.1093/gji/ggs099

Schipper, C. I., White, J. D. L., & Houghton, B. F. (2010). Syn- and post-fragmentation textures in submarine pyroclasts from Lō'ihi Seamount, Hawai'i. *Journal of Volcanology and Geothermal Research*, *191*(1-2), 93–106. https://doi.org/10.1016/j.jvolgeores.2010.01.002

Schipper, C. I., White, J. D. L., & Houghton, B. F. (2011). Textural, geochemical, and volatile evidence for a Strombolian-like eruption sequence at Lō'ihi Seamount, Hawai'i. *Journal of Volcanology and Geothermal Research*, *207*(1-2), 16–32. https://doi.org/10.1016/j.jvolgeores.2011.08.001

Shea, T., Houghton, B. F., Gurioli, L., Cashman, K. V., Hammer, J. E., & Hobden, B. J. (2010). Textural studies of vesicles in volcanic rocks: An integrated methodology. *Journal of Volcanology and Geothermal Research*, *190*(3-4), 271–289. https://doi.org/10.1016/j.jvolgeores.2009.12.003

Sparks, R. S. J. (1978). The dynamics of bubble formation and growth in magmas: a review and analysis. *Journal of Volcanology and Geothermal Research*, *3*(1–2), 1–37. https://doi.org/10.1016/0377-0273(78)90002-1

Spina, L., Cimarelli, C., Scheu, B., Di Genova, D., & Dingwell, D. B. (2016). On the slow decompressive response of volatile- and crystal-bearing magmas: An analogue experimental investigation. *Earth and Planetary Science Letters*, *433*, 44–53. https://doi.org/10.1016/j.epsl.2015.10.029

Stovall, W. K., Houghton, B. F., Gonnermann, H., Fagents, S. A., & Swanson, D. A. (2011). Eruption dynamics of Hawaiian-style fountains: The case study of episode 1 of the Kīlauea Iki 1959 eruption. *Bulletin of Volcanology*, *73*(5), 511–529. https://doi.org/10.1007/s00445-010-0426-z

Stroberg, T. W., Manga, M., & Dufek, J. (2010). Heat transfer coefficients of natural volcanic clasts. *Journal of Volcanology and Geothermal Research*, *194*(4), 214–219. https://doi.org/10.1016/j.jvolgeores.2010.05.007

van Otterloo, J., Cas, R. A. F., & Scutter, C. R. (2015). Earth-science reviews the fracture behaviour of volcanic glass and relevance to quench fragmentation during formation of hyaloclastite and phreatomagmatism. *Earth-Science Reviews*, *151*, 79–116. https://doi.org/10.1016/j.earscirev.2015.10.003

Vasseur, J., & Wadsworth, F. B. (2017). Sphere models for pore geometry and fluid permeability in heterogeneous magmas. *Bulletin of Volcanology*, *79*(11), 77. https://doi.org/10.1007/s00445-017-1165-1

Vaughan, R. G., & Webley, P. W. (2010). Satellite observations of a surtseyan eruption: Hunga Ha'apai, Tonga. *Journal of Volcanology and Geothermal Research*, *198*(1-2), 177–186. https://doi.org/10.1016/j.jvolgeores.2010.08.017

Wadsworth, F. B., Vasseur, J., Llewellin, E. W., Dobson, K. J., Colombier, M., von Aulock, F. W., et al. (2017). Topological inversions in coalescing granular media control fluid-flow regimes. *Physical Review E*, *96*(3), 033113.

Wadsworth, F. B., Vasseur, J., Llewellin, E. W., Genareau, K., Cimarelli, C., & Dingwell, D. B. (2017). Size limits for rounding of volcanic ash particles heated by lightning. *Journal of Geophysical Research: Solid Earth*, *122*, 1977–1989. https://doi.org/10.1002/2016JB013864

Walker, G. P. L., & Croasdale, R. (1971). Characteristics of some basaltic pyroclastics. *Bulletin Volcanologique*, *35*(2), 303–317. https://doi.org/10.1007/BF02596957

Wilding, M., Dingwell, D., Batiza, R., & Wilson, L. (2000). Cooling rates of hyaloclastites: Applications of relaxation geospeedometry to undersea volcanic deposits. *Bulletin of Volcanology*, *61*(8), 527–536. https://doi.org/10.1007/s004450050003

Wright, H. M. N., Cashman, K. V., Rosi, M., & Cioni, R. (2007). Breadcrust bombs as indicators of Vulcanian eruption dynamics at Guagua Pichincha volcano, Ecuador. *Bulletin of Volcanology*, *69*(3), 281–300. https://doi.org/10.1007/s00445-006-0073-6

Wright, I. C., Gamble, J. A., & Shane, P. A. (2003). Submarine silicic volcanism of the Healy caldera, southern Kermadec arc (SW Pacific): I—Volcanology and eruption mechanisms. *Bulletin of Volcanology*, *65*(1), 15–29.

Zhang, Y., & Ni, H. (2010). Diffusion of H, C, and O components in silicate melts. *Reviews in Mineralogy and Geochemistry*, *72*(1), 171–225. https://doi.org/10.2138/rmg.2010.72.5